Quadruple perovskite CaCu₃Fe₂Re₂O₁₂: A potential actuator based on a multiscale model

Zeliang Liu [a,b,c,*], Huijian Li [a,c], Xiao Yang [c], Wei Luo [b,**]

[a] Key Laboratory of Mechanical Reliability for Heavy Equipments and Large Structures of Hebei Province, Yanshan University, Qinhuangdao 066004 China
[b] Department of Physics and Astronomy, Uppsala University, Uppsala S75121, Sweden
[c] School of Civil Engineering and Mechanics, Yanshan University, Qin Huangdao, 066004 China

ARTICLE INFO

ABSTRACT

In this study, the magnetic structure of $CaCu_3Fe_2Re_2O_{12}$ is analyzed combined on a macro to micro-scale. To combine first-principles calculations and finite element methods, the magnetic properties, Young's modulus and Poisson's ratio are used as input parameters in the finite element methods calculations. As a function of applied magnetic field and actuator structure, the energy loss and magnetostrictive coefficient of an magnetostrictive actuator are identified. When the voltage and frequency are specified, a small bar radius and narrow air gap are preferred for a high magnetostrictive coefficient. The total range of simulation parameters results in a large magnetostrictive coefficient of 2700 ppm, which is higher than the one for Tb-Dy-Fe alloys. According to our results, $CaCu_3Fe_2Re_2O_{12}$ can be designed to be used as actuators by controlling the structures and applying magnetic fields.

1. Introduction

In ferromagnetic materials, one of the most important properties is the magnetostrictive (MS) coefficient. This determines how the material will change in shape and size during magnetization. It was first observed in iron by James [1]. The functional materials have been used to manufacture devices such as transducers, micro-displacement drivers, and noise and vibration control systems [2]. There are many applications for spin-polarized materials in electronic and magnetic technology [3].

Double-perovskites are considered to be the most promising magnetic resonance material due to their high curie transition temperature and magnetic resonance at low fields [4,5]. An orderly double-perovskite structure $A_2BB'O_6$ is characteristic of transition metal oxides [6,7], where A is an alkali-earth metal; B and B′ represent the transition metals. By introducing magnetic interactions in addition to B-B couplings, various fascinating properties were observed in a quadruple perovskite structure oxide [8]. As an example, if the B-site is nonmagnetic ions Ge, Sn, and Ti, the interaction in structure produces ferromagnetic behavior for B = Ge and Sn, while it produces antiferromagnetic behavior for B = Ti [9,10]. When is at A′-site and B-site is

magnetic ions Mn, the coupling between Cu spins at A′-site antiferromagnetically and magnetic spins at B-site results in ferrimagnetic behavior [11]. When the magnetic field is low, there is a large magnetic resonance [12].

For an actuator materials, large magnetostrictive strain value, high Curie temperature, good frequency response characteristics and high energy density are required. To obtain the combined advantages of an A-site-ordered $AA'_3B_4O_{12}$ and perovskite and $A_2BB'O_6$ double perovskite, the A- and B-site-ordered quadruple perovskite oxide $AA'_3B_2B'_2O_{12}$ were explored [13,14]. An A- and B-site-ordered quadruple perovskite oxide, $CaCu_3Fe_2Re_2O_{12}$, has been reported with a large magnetization of 8.7 μ_B f.u.$^{-1}$ and a very high Curie temperature of 560 K [15]. Therefore, this material indicates potential magnetostrictive applications.

Modeling the properties and functions of materials and processes at multiscales has shifted from descriptive to predictive in recent years [16,17]. A multiscale model can be used for discovering mechanisms, and an analytical approach can be used to characterize functional materials [18,19]. Typically, ab initio methods are used at small scales [20]. Using these methods is the key to successful multiscale models because they reveal the nature of bonds and fundamental properties [21].

* Corresponding author at: Key Laboratory of Mechanical Reliability for Heavy Equipments and Large Structures of Hebei Province, Yanshan University, Qinhuangdao 066004 China.
** Corresponding author.
E-mail addresses: liuzeliang@ysu.edu.cn (Z. Liu), wei.luo@physics.uu.se (W. Luo).

In the present work, the magnetic-structure calculations of CaCu$_3$Fe$_2$Re$_2$O$_{12}$ are performed based on the first principles and finite element method (FEM). The mechanical properties are determined by performing first-principles calculations. Through the equivalent set of magnetic and electrical quantities, the MS effect is determined by performing the piezoelectric coupling calculations based on the finite element method. The energy loss and MS coefficient as a function of applied magnetic field and actuator structure are obtained.

The rest of this paper is organized as follows. Section 2 introduces the computational details for the potential application of CaCu$_3$Fe$_2$Re$_2$O$_{12}$ as a transducer, detailing first-principles theoretical calculations and FEM applied on MS actuators. Then in Section 3, the results and discussion are presented, including the Crystal structure of CaCu$_3$Fe$_2$Re$_2$O$_{12}$, FEM models, effect of external magnetic field and actuator structure parameters for the actuator. Finally conclusions are drawn in Section 4, together with some discussion of potential future work.

2. Computational details

In order to explore the potential application of CaCu$_3$Fe$_2$Re$_2$O$_{12}$ as a transducer, the MS coefficient and energy loss of the material under the action of electromagnetic field are studied. The electromagnetic and mechanical properties of CaCu$_3$Fe$_2$Re$_2$O$_{12}$ which were used to the transducer were characterized by microscopic calculation. Then, the MS performance of the transducer is calculated by the finite element method. Therefore, the process is a micro-macro combination and magnetic structure coupling calculations.

2.1. First-principles theoretical calculations

In this work, the first-principles plane-wave calculations were performed based on density functional theory (DFT) implemented in the Vienna Ab Initio Simulations Package (VASP) [22]. The Perdew-Burke-Ernzerhof (PBE) [23] generalized gradient approximation (GGA) [24] exchange-correlation functional was used to describe the electronic exchange-correlation effects. The valence states of Ca, Cu, Fe, Re and O are $3p^6 4 s^2$, $3d^{10} 4 s^1$, $3d^7 4 s^1$, $5d^6 6 s^1$ and $2 s^2 2p^4$, respectively. To describe the on-site Coulomb interaction between d electrons of the Fe and Re atoms, a PBE+U method was employed for the Fe and Re d orbitals with U values being set at 4.0 eV [15]. The plane-wave energy cutoff has been converged at 460 eV where the ground state total energy is approximately deviated within 1 meV/atom. The total energy and force calculations were converged to within 10^{-6} eV and 0.01 eV/Å, respectively. The $7 \times 7 \times 7$ Gamma k-mesh for Brillouin zone integration was used for structure optimization.

The elastic constants were calculated based on the strain-stress approach [25], in which the energy cutoff was set up to 600 eV. For Pn$\overline{3}$ structure, there are three independent elastic constants, C_{11}, C_{12} and C_{44} [26,27]. The bulk modulus and share modulus are calculated based on Hill [28] approximation which is the average of the Voigt [29] and Reuss [30] approximation. For a cubic crystal, the bulk modulus in Voigt and Reuss approximations (B_V and B_R) is calculated by,

$$B_v = B_R = \frac{1}{3}(C_{11} + 2C_{12}) \tag{1}$$

The shear modulus in Voigt and Reuss approximations (G_V and G_R) are,

$$G_v = \frac{1}{5}(C_{11} - C_{12} + 3C_{44})$$
$$G_R = \frac{5(C_{11} - C_{12})C_{44}}{4C_{44} + 3(C_{11} - C_{12})} \tag{2}$$

For the macro finite element model, the material is considered to be an isotropic homogeneous polycrystalline material. The bulk modulus B and shear modulus G of the CaCu$_3$Fe$_2$Re$_2$O$_{12}$ polycrystalline based on Hill approximations were obtained by,

$$B = \frac{1}{2}(B_V + B_R)$$
$$G = \frac{1}{2}(G_V + G_R) \tag{3}$$

Then, the Young's modulus E and Poisson's ratio ν can be determined by,

$$E = \frac{9BG}{3B + G}$$
$$\nu = \frac{3B - 2G}{6B + 2G} \tag{4}$$

2.2. FEM applied on MS actuators

The magnetic-structural calculations were performed based on the finite element method (FEM) implemented in ANSYS [31]. Maxwell equation [32] is the foundation for studying the macro electric and magnetic fields. The differential form is as follows:

$$\begin{cases} \nabla \times H = J + \dfrac{\partial J}{\partial t} \\ \nabla \times E = -\dfrac{\partial B}{\partial t} \\ \nabla \bullet D = \rho \\ \nabla \bullet B = 0 \end{cases} \tag{5}$$

where, ∇ is the differential operator; H is magnetic field intensity vector; J is conduction current density vector; t is the time coordinate; E is electric field intensity vector; B is flux density vector, which can be expressed as the product of vacuum permeability μ_0 and H; D is electric displacement vector; t is time; ρ is free charge density; The ∂ is partial derivative operator; The $\times$ and $\bullet$ are the divergence operator and curl operator, respectively.

The magnetic field formed by a constant current is a constant magnetic field which can be expressed as:

$$\begin{cases} \dfrac{\partial D}{\partial t} = 0 \\ \dfrac{\partial B}{\partial t} = 0 \end{cases} \tag{6}$$

Introducing vector magnetic potential A to satisfy the following equation:

$$B = \nabla \times A \tag{7}$$

Then, the finite element equation of the magnetic field of the drive coil is obtained as follows:

$$\nabla^2 A = -\mu_0 J \tag{8}$$

The linear behavior for piezoelectric materials is related to the matrix form of the constitutive equations [33]:

$$\sigma = c^E S - eE$$
$$D = eS + \varepsilon^s E \tag{9}$$

where, σ is stress. D is electric displacement. S is strain; E is electric field intensity; c^E is elastic coefficient under constant electric field; e is piezoelectric stress constant; ε^s is dielectric constant under constant strain. The physical mechanism of MS effect and piezoelectric effect is the same. The linear behavior for MS materials are related to the matrix form of the constitutive equations:

$$\sigma = c^H S - \beta H$$
$$B = \beta S + \mu^S H \tag{10}$$

where, H is magnetic field strength; B is magnetic flux density; c^H is

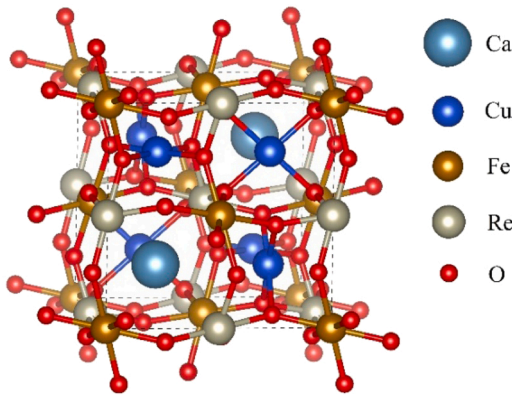**Fig. 1.** Crystal structure of $CaCu_3Fe_2Re_2O_{12}$.

Table 1
The structure parameters and elastic properties of $CaCu_3Fe_2Re_2O_{12}$.

	Present work	Experiment
Lattice parameter (Å)	7.379	7.447[15]
magnetic moment (μ_B)	8.4	8.7[15]
Bulk modulus (GPa)	221.6	
shear modulus (GPa)	100.6	
Young's modulus (GPa)	262.1	
Poisson's ratio	0.30	

elastic coefficient under constant magnetic field strength; β is MS strain constant, which represents the flux density change caused by unit strain; μ^S is permeability under constant strain. The finite element governing equation for the MS coefficient was given:

$$\begin{bmatrix} [M] & [0] \\ [0] & [0] \end{bmatrix}\begin{bmatrix} [\ddot{u}] \\ [\ddot{A}] \end{bmatrix} + \begin{bmatrix} [C] & [0] \\ [0] & [0] \end{bmatrix}\begin{bmatrix} [\dot{u}] \\ [\dot{A}] \end{bmatrix} + \begin{bmatrix} [K] & [K_m] \\ [K_m]^T & [K_u] \end{bmatrix}\begin{bmatrix} [u] \\ [A] \end{bmatrix} = \begin{bmatrix} [F] \\ [\Phi] \end{bmatrix}$$

(11)

where, $[M]$ is mass matrix; $[C]$ is damping matrix; $[K]$ is stiffness matrix; $[K_u]$ is permeability matrix which is determined by μ^S of material and element interpolation function; $[K_m]$ is MS coupling matrix which is determined by the piezomagnetic coefficient matrix $[\beta]$ of the material and the interpolation function of the element; $[u]$ is structural displacement vector; $[F]$ is load force vector, $[A]$ is ampere-turn vector and $[\Phi]$ is magnetic flux vector through cross section.

According to the Eqs. (8) and (11), the Maxwell force, power loss and deformation of the structure under magnetic field can be obtained.

3. Results and discussion

3.1. Crystal structure of $CaCu_3Fe_2Re_2O_{12}$

The crystal structure of $CaCu_3Fe_2Re_2O_{12}$ with space group $Pn\overline{3}$ (no. 201) is plotted in Fig. 1. In this structure, Ca atoms are positioned at 2a (1/4 1/4 1/4) sites, Cu atoms are positioned at 6d (1/4 3/4 3/4) sites, Fe atoms are positioned at 4b (0 0 0) sites, Re atoms are positioned at 4c (1/2 1/2 1/2) sites, and O atoms are positioned at 24 h (0.45 0.75 0.07) sites.

Table 1. The structure parameters and elastic properties of $CaCu_3$-$Fe_2Re_2O_{12}$. We obtained excellent agreement with the experiment for both the equilibrium lattice constants and the magnetic moment (both differ by less than 3.5%, as shown in Table 1). The good agreement of the results proves that our calculation is accurate. The calculation condition is absolute zero while the experiment is at room temperature, which is the main reason for lattice error.
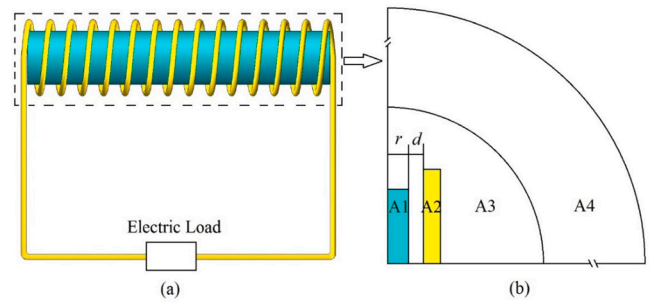

Fig. 2. Actuator structure (a) Diagram of MS actuator. MS bar in green color, copper coil in yellow color. (b) 2D finite element model schematic. A1 denotes the bar area, the size of bar radius is r; A2 denotes the copper coil which is used to couple current freedom and voltage drop load, the size of air gap between A1 and A2 is d; A3 denotes air zone; A4 denotes far-field region to correctly reflect the phenomenon of magnetic leakage.

Table 2
The relationship between the induced magnetic flux density (B) and the external applied magnetizing force (H) of $CaCu_3Fe_2Re_2O_{12}$.

H (kA/m)	B (T)	H (kA/m)	B (T)	H (kA/m)	B (T)	H (kA/m)	B (T)
3.6	0.0336	61.5	0.3906	250.2	0.8000	742.5	1.4366
16.0	0.1390	73.8	0.4510	307.6	0.8797	795.8	1.5046
24.6	0.1943	90.2	0.5016	369.2	0.9600	954.9	1.7046
32.8	0.2496	119.0	0.5691	525.0	1.1589	1193.7	2.0046
41.0	0.3048	147.7	0.6337	598.9	1.2531	1591.5	2.5046
53.3	0.3518	196.9	0.7195	701.4	1.3835		

3.2. FEM models of actuator

According to Grunwald and A.G Olabi [34], there are four driving magnetic field forms of the MS actuator. Fig. 2(a) shows the simplest MS actuator structure called TC structure. It is taken as an example to calculate the MS properties of $CaCu_3Fe_2Re_2O_{12}$ by finite element simulation. There are four main factors affecting magnetic induction intensity: radius of bar r, the voltage applied to the copper coil V, size of air gap d and frequency of external magnetic field f. Because of the symmetry of MS actuator, this structure can be simplified to two-dimensional (2D) axisymmetric analysis. The 2D model is shown in Fig. 2(b). The element type for the bar area (A1), the copper coil (A2) and the air zone (A3) is PLANE53, which is a two-dimensional 8-node magnetic solid element. The element type for the far-field region (A4) is INFIN110, which is a two-dimensional 4-node infinite quadrilateral element. All areas are meshed into quadrilateral elements. Element convergence calculation shows that the strain difference on the top of A1 converged to within 10^{-3}. Applying Dirichlet and Neumann boundary conditions [35] to the y-axis nodes and the far-field outer boundary nodes, respectively. Planar symmetry constraints imposed on x-axis nodes. The relative permeability of air and copper coil is 1 (one). The resistivity of copper coil and $CaCu_3Fe_2Re_2O_{12}$ are 1.75 e^{-8} $\Omega \bullet m$ and 1.00 e^{-4} $\Omega \bullet m$, respectively.

The relationship between the induced magnetic flux density (B) and the external applied magnetizing force (H) of $CaCu_3Fe_2Re_2O_{12}$ is shown in Table 2. The magnetic field dependence of magnetization can be seen in reference [15]. The relationship of B and H can be obtained according to the equation:

$$B = \mu_0(H + M)$$

(12)

where, $\mu_0 = 4\pi \times 10^{-7}$ H/m. Table 2 indicates that greater external applied magnetizing force is required to achieve the large magnetic flux density than terfenol-D [36,37].
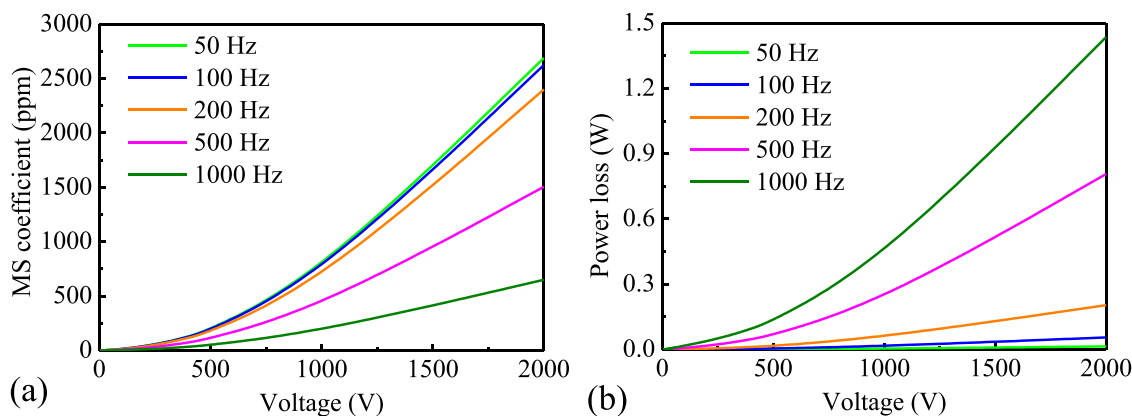
Fig. 3. The MS coefficient and power loss as a function of voltage with different frequency.
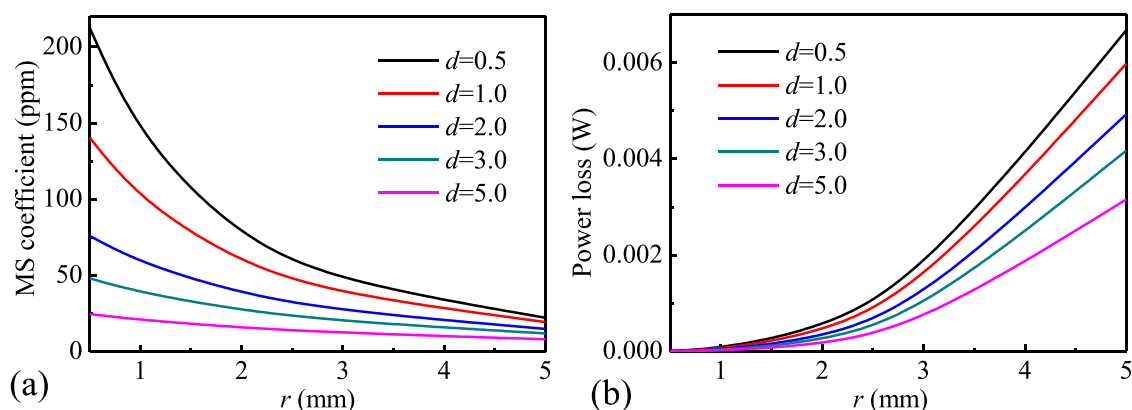

Fig. 4. The MS coefficient and power loss as a function of bar radius with different air gap.

3.3. Effect of external magnetic field

Fig. 3 shows the MS coefficient and power loss as a function of voltage with different frequencies when the bar radius is 2 mm and the air gap is 2 mm. It shows that the MS coefficient as well as power loss increase with the increase of voltage. Fig. 3(a) shows that the higher the frequency is, the smaller the MS coefficient is, and the slower the coefficient increases with the voltage. Fig. 3(b) shows that the higher the frequency is, the greater the power loss is, and the faster the power loss increases with the voltage. The results suggest that high voltage leads to a high MS coefficient but also leads to high power loss. Moreover, the low frequency is preferred to large MS coefficient and low power loss. Within the voltage range of simulation, the MS coefficient is up to 2700 ppm higher than that of Tb-Dy-Fe alloys [38].

3.4. Effect of structural parameters

The structural parameters also affect the properties of materials in magnetic fields. Fig. 4 shows the MS coefficient and power loss as a function of bar radius with different air gap when the voltage is 200 V and the frequency is 50 Hz. Fig. 4(a) shows that the MS coefficient decreases with the increase of the bar radius. Moreover, the MS coefficient decreases with the increase of the air gaps. Fig. 4(b) shows that the power loss increases with the increase of the bar radius. Moreover, the power loss decreases with the increase of the air gap. The air gap increases from 0.5 mm to 5 mm, the power loss decreases in 5 mW. The results suggest that the small bar radius and narrow air gap are recommended for design.

4. Conclusions

As a result, the magnetic-structural coupling of $CaCu_3Fe_2Re_2O_{12}$ in the applied magnetic field was investigated using a multiscale model that begins with ab initio predictions and concludes with a crystal-mechanical finite element method. The mechanical properties of $CaCu_3Fe_2Re_2O_{12}$ were studied by ab initio calculations using density functional theory. In terms of Young's modulus and Poisson's ratio, the values are 262.1 GPa and 0.30, respectively. A finite element analysis of this material indicates that a low frequency and high voltage are ideal for obtaining a significant MS coefficient. When the voltage is up to 2000 V and the frequency is 50 Hz, the MS coefficient can reach as high as 2700 ppm. It is recommended to design the bar with a narrow air gap and a tiny radius. Based on the results, this material may prove useful for transducers.

CRediT authorship contribution statement

Zeliang Liu: Conceptualization, Methodology, Software, Investigation, Formal analysis, Data Curation, Writing – review & editing, **Huijian Li:** Supervision, review & editing. **Xiao Yang:** Software, Data Curation. **Wei Luo:** Conceptualization, Supervision, Writing – review & editing.

Declaration of Competing Interest

The authors declare that they have no known competing financial interests or personal relationships that could have appeared to influence the work reported in this paper.

References

[1] J.P. Joule, XVII. On the effects of magnetism upon the dimensions of iron and steel bars, Lond., Edinb., Dublin Philos. Mag. J. Sci. 30 (1847) 76–871847, https://doi.org/10.1080/14786444708645656.

[2] H. Jafari, A. Ghodsi, S. Azizi, M.R. Ghazavi, Energy harvesting based on magnetostriction, for low frequency excitations, Energy 124 (2017) 1–8, https://doi.org/10.1016/j.energy.2017.02.014.

[3] R.J. Celotta, D.T. Pierce, Polarized electron probes of magnetic surfaces, Science 234 (1986) 333–340, https://doi.org/10.1126/science.234.4774.333.

[4] J. Liu, et al., Realization of magnetostructural coupling by modifying structural transitions in MnNiSi-CoNiGe system with a wide Curie-temperature window, Sci. Rep. 6 (2016) 1–8, https://doi.org/10.1038/srep23386.

[5] Y.K. Wakabayashi, et al., Ferromagnetism above 1000 K in a highly cation-ordered double-perovskite insulator Sr_3OsO_6, Nat. Commun. 10 (2019) 1–8, https://doi.org/10.1038/s41467-019-08440-6.

[6] D. Serrate, J.M. De Teresa, M.R. Ibarra, Double perovskites with ferromagnetism above room temperature, J. Phys. -Condens. Mat. 19 (2006), 023201, https://doi.org/10.1088/0953-8984/19/2/023201.

[7] T. Saha-Dasgupta, Magnetism in double perovskites, J. Supercond. Nov. Magn. 26 (2013) 1991–1995, https://doi.org/10.1007/s10948-012-1920-7.

[8] Y. Shimakawa, A-site-ordered perovskites with intriguing physical properties, Inorg. Chem. 47 (2008) 8562–8570, https://doi.org/10.1021/ic800696u.

[9] H. Shiraki, et al., Ferromagnetic cuprates $CaCu_3Ge_4O_{12}$ and $CaCu_3Sn_4O_{12}$ with A-site ordered perovskite structure, Phys. Rev. B. 76 (2007), 140403, https://doi.org/10.1103/PhysRevB.76.140403.

[10] J.G. Cheng, J.S. Zhou, J.B. Goodenough, Y.T. Su, Y. Sui, Evidence of three-dimensional Ising ferromagnetism in the A-site-ordered perovskite $CaCu_3Ge_4O_{12}$, Phys. Rev. B. 83 (2011), 212403, https://doi.org/10.1103/PhysRevB.83.212403.

[11] Z. Zeng, M. Greenblatt, J.E. Sunstrom IV, M. Croft, S. Khalid, Giant magnetoresistance in $CaCu_3Mn_4O_{12}$-based oxides with perovskite-type structure, J. Solid State Chem. 147 (1999) 185–198, https://doi.org/10.1006/jssc.1999.8212.

[12] X.J. Liu, et al., A first-principles study of the different magnetoresistance mechanisms in $CaCu_3Mn_4O_{12}$ and $LaCu_3Mn_4O_{12}$, J. Mater. Chem. 16 (2006) 4243–4248, https://doi.org/10.1039/B609895A.

[13] S.H. Byeon, S.S. Lee, J.B. Parise, P.M. Woodward, Nam Hwi Hur, et al., New ferrimagnetic oxide $CaCu_3Cr_2Sb_2O_{12}$: high-pressure synthesis, structure, and magnetic properties, Chem. Mater. 17 (2005) 3552–3557, https://doi.org/10.1021/cm050397b.

[14] S.S. Ahmed, G.D. Ngantso, L. Bahmad, A. Benyoussef, A.E. Kenz, Phase diagrams and magnetic properties of $CaCu_3Fe_2Os_2O_{12}$ quadruple perovskite: Monte Carlo study, Phys. Lett. A. 382 (2018) 186–192, https://doi.org/10.1016/j.physleta.2017.09.025.

[15] W. Chen, et al., A half-metallic A-and B-site-ordered quadruple perovskite oxide $CaCu_3Fe_2Re_2O_{12}$ with large magnetization and a high transition temperature, Nat. Commun. 5 (2014) 3909, https://doi.org/10.1038/ncomms4909.

[16] S.I. Yengejeh, S.A. Kazemi, W. Wen, Y. Wang, Multiscale numerical simulation of in-plane mechanical properties of two-dimensional monolayers, RSC Adv. 11 (2021) 20232–20247, https://doi.org/10.1039/D1RA01924D.

[17] L. Niu, et al., A ductile fracture criterion under warm-working conditions based on the multiscale model combining molecular dynamics with finite element methods, Int. J. Plast. 149 (2022), 103185, https://doi.org/10.1016/j.ijplas.2021.103185.

[18] P.S. Branicio, et al., Elastic interaction of hydrogen atoms on graphene: a multiscale approach from first principles to continuum elasticity, . *Phys. Rev. B* 94 (2016), 165420, https://doi.org/10.1103/PhysRevB.94.165420.

[19] L. Debbichi, et al., Mixed valence perovskite $Cs_2Au_2I_6$: a potential material for thin-film Pb-free photovoltaic cells with ultrahigh efficiency, Adv. Mater. 30 (2018) 1707001, https://doi.org/10.1002/adma.201707001.

[20] B. Mortazavi, et al., First-principles multiscale modeling of mechanical properties in graphene/borophene heterostructures empowered by machine-learning interatomic potentials, Adv. Mater. 33 (2021) 2102807, https://doi.org/10.1002/adma.202102807.

[21] P. Aghdasi, R. Ansari, S. Rouhi, Sh Yousefi, A DFT-based finite element approach for studying elastic properties, buckling and vibration of the arsenene, J. Mol. Graph. Model. 101 (2020), 107725, https://doi.org/10.1016/j.jmgm.2020.107725.

[22] G. Kresse, J. Furthmüller, Efficient iterative schemes for ab initio total-energy calculations using a plane-wave basis set, Phys. Rev. B 54 (1996) 169, https://doi.org/10.1103/PhysRevB.54.11169.

[23] J.P. Perdew, K. Burke, M. Ernzerhof, Generalized gradient approximation made simple, Phys. Rev. Lett. 77 (1996) 3865, https://doi.org/10.1103/PhysRevLett.77.3865.

[24] G. Kresse, D. Joubert, From ultrasoft pseudopotentials to the projector augmented-wave method, Phys. Rev. B. 59 (1999) 1758, https://doi.org/10.1103/PhysRevB.59.1758.

[25] Y. Le Page, P. Saxe, Symmetry-general least-squares extraction of elastic data for strained materials from ab initio calculations of stress, Phys. Rev. B. 65 (2002), 104104, https://doi.org/10.1103/PhysRevB.65.104104.

[26] Z. Wu, et al., Crystal structures and elastic properties of superhard IrN_2 and IrN_3 from first principles, Phys. Rev. B 76 (5) (2007), 054115, https://doi.org/10.1103/PhysRevB.76.054115.

[27] F. Mouhat, F.X. Coudert, Necessary and sufficient elastic stability conditions in various crystal systems, Phys. Rev. B 90 (22) (2014), 224104, https://doi.org/10.1103/PhysRevB.90.224104.

[28] R. Hill, The elastic behaviour of a crystalline aggregate, Proc. Phys. Soc. Sect. A 65 (1952) 349, https://doi.org/10.1088/0370-1298/65/5/307.

[29] W. Voigt, A determination of the elastic constants for beta-quartz lehrbuch de kristallphysik, Terubner Leipz. 40 (1928) 2856–2860.

[30] A. Reuss, Berechnung der fließgrenze von mischkristallen auf grund der plastizitätsbedingung für einkristalle, ZAMM-J. Appl. Math. Mech. /Z. für Angew. Math. und Mech. 9 (1929) 49–58, https://doi.org/10.1002/zamm.19290090104.

[31] H.H. Lee, ISBN 978-1-63057-088-0, Finite Element Simulations with ANSYS Workbench 18[M], 50, SDC publications, 2018.

[32] J.C. Maxwell, A dynamical theory of the electromagnetic field, Philos. Trans. R. Soc. Lond. 155 (1865) 459–512, https://doi.org/10.1098/rstl.1865.0008.

[33] H. Talleb, Z. Ren, Finite-element modeling of a magnetoelectric energy transducer including the load effect, IEEE T. Magn. 51 (2015) 1–5, https://doi.org/10.1109/TMAG.2014.2357492.

[34] A. Grunwald, A.G. Olabi, Design of a magnetostrictive (MS) actuator, Sens. Actuat. A-Phys. 144 (2008) 161–175, https://doi.org/10.1016/j.sna.2007.12.034.

[35] T. Nakata, N. Takahashi, K. Fujiwara, M. Sakaguchi, 3-D open boundary magnetic field analysis using infinite element based on hybrid finite element method, IEEE T. Magn. 26 (1990) 368–370, https://doi.org/10.1109/20.106330.

[36] M. Ghodsi, S. Mirzamohamadi, S. Talebian, et al., Analytical, numerical and experimental investigation of a giant magnetostrictive (GM) force sensor, Sens. Rev. 35 (2015) 357–365, https://doi.org/10.1108/SR-12-2014-0760.

[37] S. Talebian, Y. Hojjat, M. Ghodsi, et al., Study on classical and excess eddy currents losses of Terfenol-D, J. Magn. Magn. Mater. 388 (2015) 150–159, https://doi.org/10.1016/j.jmmm.2015.04.033.

[38] J.J. Liu, et al., Structural, magnetic and magnetostrictive properties of $Tb_{0.2}Pr_{0.8}(Fe_{0.4-x}Co_{0.6+x})_{1.93}$ alloys, J. Phys. D. -Appl. Phys. 39 (2006) 243–247, https://doi.org/10.1088/0022-3727/39/2/002.